MULTISCALE SIMULATION OF NANOPARTICAL TRANSPORT IN DEFORMABLE TISSUE DURING AN INFUSION PROCESS IN HYPERTHERMIA TREATMENT OF CANCERS

Ronghui Ma
Di Su
Liang Zhu

ABSTRACT

A multiscale model was developed in this study to investigate the behavior of nanoparticle transport in tissues after intratumoral infusion. It consists of a particle trajectory tracking model that considers particle-surface interactions, and a macroscale model for fluid flow and nanoparticle transport through deformable tissues. The multiscale model was used to quantify the effects of tumor deformation and particle binding to the cell surface on the particle distribution. The results show that the rate of particle binding to the cellular structure can be reduced by increasing the local interstitial fluid velocity, tissue porosity, and surface charge of the particles. Tissue deformation induced by the infusion pressure causes backflow and change in tissue porosity near the needle tip, which substantially affects the distribution and penetration depth of the nanoparticles. Simulations were performed using a variety of infusion conditions to quantify the effects of infusion rates, needle sizes, tissue elastic properties, and injection amounts on the spatial distribution of nanoparticles in tumors.

1. INTRODUCTION

Hyperthermia has been used in a variety of therapeutic procedures of patients with cancers in the past several decades [13]. It is suitable for patients diagnosed with

previously unresectable tumors, or for patients who are looking for an alternative to costly and risky surgical procedures. In hyperthermia, thermal energy delivered to tumors raises the tumor temperature above 43°C for durations of more than 60 minutes. It has been reported that such elevated temperatures may produce a heat-induced cytotoxic response and/or enhance the cytotoxic effects of radiation and drugs. Both the direct cell-killing effects of heat and the sensitization to other therapeutic agents by heat are phenomena strongly associated with the distribution of the temperature elevations and duration of heating.

Nanoparticles have found important applications in novel hyperthermia treatment of cancers due to their ability to generate impressive level of heat when excited by an external magnetic field or laser irradiation [56]. For example, magnetic nanoparticles delivered in tumors can induce localized heating when agitated by an alternative magnetic field. The heat generation is mainly attributed to the Néel relaxation and/or Brownian motion of the particles. Iron oxides magnetite Fe_3O_4 and maghemite γ-Fe_2O_3 nanoparticles are the most employed to date due to their biocompatibility [17, 29, 35]. Smaller particles (10-40 nm) are preferred in magnetic hyperthermia applications due to their ability to produce impressive level of heating in relatively low magnetic fields [23]. In laser photothermal therapy where heat generation in tumors is induced by near infrared (NIR) laser irradiation on the surface, the inclusion of golden nanoshells/nanorods in the tumor leads to maximized absorption of the laser energy to elevate local tumor temperatures [5, 12, 41]. Previous studies have demonstrated that the usage of golden nanoshells/nanorods can enhance laser energy absorption by several orders of magnitude compared to some traditional dyes, such as indocynine green dye [52]. Despite the demonstrated potential of various types of nanoparticles in hyperthermia treatment, there exist a number of challenges to be addressed before their widespread applications in clinical studies. One leading issue is the limited knowledge and understanding of nanoparticle distribution and anticipated temperature elevations in tumors. Since nanoparticles serve as the heat generating agents, the efficacy of the treatment depends largely upon the spatial distribution of the nanoparticles in tumors. The lack of control of nanoparticle distribution may lead to under-dosage of heating in the tumor or overheating of the normal tissue.

Two techniques are currently used to deliver nanoparticles to a tumor. The first is systemic (venous) injection of dispersed nanoparticles in biocompatible solution. The majority of the nanostructures eventually accumulate in tumors due to the small size of the nanostructures and the leaky nature of tumor vasculature. The efficiency of the systemic delivery can be improved by coating the nanostructures with some chemicals that target tumor cells [60]. However, systemic administration is not suitable for poorly perfused, large-sized, and irregular-shaped tumors. The second approach, which is the focus of the current study, is direct infusion, also referred to as intratumoral infusion or convection enhanced delivery. It is an important technique to deliver a variety of nanostructures in tumors by continuous injection of nanofluid under positive pressure gradient [2, 17, 18, 32]. It is so far the best method available for distributing large therapeutic agents in tumors in that it allows those agents to overcome some of the obstacles such as interstitial fluid pressure or brain blood barrier, through enhanced convective transport [34]. This approach has been used to deliver ferrofluid to treat

tumors in liver [32] and breast [17, 18]. In case of an irregular shaped tumor, multiple-site injections can be exploited to cover the entire targeted region [50].

Quantitative characterization of the nanoparticle distribution in tissue after infusion is very limited due to the opaque nature of the tissue and insufficient techniques to quantify the nanoparticle concentration distribution. Salloum et al. [48, 49] studied the injection of ferrofluid in semi-transparent agarose gels and demonstrated that the distribution volume of ferrofluid is sensitive to both the injection rate and the agarose gel properties. In addition, a higher infusion rate yields a more irregular shaped nanofluid distribution in the gel. In the same studies, heating patterns of the magnetic nanoparticles injected in gels/tissues were quantified by placing the gels/tissues in an alternative magnetic field and measuring the Specific Absorption Rate (*SAR*) at multiple locations. These studies suggested that the *SAR* distributions can be used to characterize the nanoparticle concentration based on the hypothesis that heating distribution is solely dependent on the spatial distribution of the nanoparticles when other parameters such as the type of the ferrofluid, the properties of the particles, the properties of the gel/tissue, and the strength of the magnetic field are fixed. The non-uniform *SAR* distributions obtained in these studies illustrate a heterogeneous nanoparticle distribution in gels/tissues [48, 49]. A Gaussian distribution of *SAR* was proposed based on fitting the experimental measurement. Although a qualitative relation among the injection parameters, gel properties, particle distribution, and heat generation is established, the understanding of the nanofluid and nanoparticle transport in gels/tissue and its dependence on the major injection parameters remains poorly understood.

The transport of nanoparticles in biological tissues during an infusion is a complex process that involves nanofluid flow through deformable tissues, advection of particles in the porous structures, particle binding to the cellular structure, and interactions among the particles. When a nanofluid is infused through a needle, the shape and volume of the nanofluid distribution in a tumor is largely dependent on the established velocity field, which is determined by both hydraulic characteristics of the tissue as well as the elastic response of the tissue to the infusion pressure. As the particles travel in the interstitial space, some can bind to the cell surface, causing nanoparticle deposition on the cellular structure. The deposition rate is affected by the interstitial fluid velocity and tissue structure as well as the characteristics of the particles. Nanofluid flow and particle binding to the cellular structures are two interrelated mechanisms having substantial influence on nanoparticle distribution during an infusion process.

Previous studies of direct infusion for drug delivery show that infusion can induce deformation in tissues which in turn changes the hydraulic conductivity of tumor tissues by altering the size and connectedness of the aqueous pathways [22, 34]. Tissue deformation can also affect nanoparticle transport because it changes the effective pore size of the extracellular structure [37]. McGuire et al. [34] developed a one-dimensional poroelastic model to describe the non-homogeneous tissue deformation. Chen et al. [8] conducted a combined experimental and theoretical study of the poroelasticity in brain tissue equivalent phantom gels to characterize the influence of gel deformation on the infusion pressure, gel matrix dilation, and pore fraction. However, this study is limited to soft gels and low infusion rates in the range of 0.5 to 10 µl/min. Ivanchenko et al. [21]

measured the deformation of gel matrix due to fluid infusion and analyzed the changes in hydraulic conductivity and porosity close to the catheter tip. The results were obtained with brain tissue equivalent phantom gels and a single infusion rate of 5 μl/min. Tissue deformation also contributes to the formation of backflow of the infusate along the needle track. Backflow is considered an important issue for enhanced convection delivery of therapeutic agents in brain tumors [2]. Morrison et al. [36] and Raghavan et al. [42] derived a simplified analytical model to quantify the backflow distance as a function of infusion parameters and tissue properties. Although the analytical solution provides valuable insight into the process, it involves bold assumptions and does not give prediction of the shape of the infusate distribution.

The convection and diffusion of large therapeutic agents such as antibodies and nucleotides by pressure-driven intratumoral infusion has been extensively studied in the past several decades [6, 11, 22, 33, 61]. However the existing theory is not readily applicable to nanoparticles because the nano-sized particles are associated with strong surface interactions that could lead to particle binding on the cell surface. Su et al. [54] conducted a multi-scale study of nanoparticle transport in biological tissues during an injection process. This model predicts nanoparticle deposition on the cellular structure via a trajectory tracking analysis considering particle-cell interactions. Nanoparticle penetration depths predicted by this multi-scale modeling are at the same order of magnitude with those indicated by experimentally measured *SAR* distributions. This study suggests that nanoparticle deposition on the extracellular structure is a leading factor for the non-uniform particle distribution in the porous medium. This model is one-dimensional and the effects of tissue deformation on the particle transport are not considered. Neeves et al. [37] attempted to enhance penetration depth of infused polymer nanoparticles (54 nm) by dilation and degradation of the brain extracellular matrix. It was found that dilating the extracellular spacing by pre-infusion of a buffer solution offers an effective means to enlarge the nanoparticle distribution volume.

Despite the existing numerical and experimental studies of the direct infusion process, the understanding of nanoparticle transport in deformable tissue is very limited. The objective of the current study is to investigate the interrelated mechanisms of nanofluid transport in tumors. Presented in this paper is a multi-scale model that considers fluid flow and deformation of tissue during an infusion process, particle interaction with the cellular structure, and nanoparticle advection and deposition in tissues. The integration of the three components allows one to study the nanoparticle transport behavior during an infusion process. The influence of the deformation induced backflow and change in porosity on particle distribution was quantified under a variety of process conditions. Parametric studies were also performed to examine the effects of infusion rates, infusion volumes, needle sizes, and tissue properties on nanoparticle concentration distribution.

2. THE MATHEMATICAL MODEL

The behavior of nanoparticle transport in biological tissues stems from the complex chemicophysical processes occurring on largely disparate temporal and spatial scales. The resulting nanoparticle distribution is dependent not only on the particle advection, diffusion, and deposition in the porous structure, but also on the mechanical response of

tissue to the infusion pressure. Specifically, the formation of backflow and the change of porosity during an infusion process can affect nanofluid distribution and rate of the particle binding to the cell surface. In this study, the nanoparticle transport in biological tissues during an intratumoral infusion is described by a multi-scale model that consists of three major components: (a) a poroelastic model for fluid flow through tissue and tissue deformation; (b) nanoparticle convection, diffusion, and deposition in tissues; and (c) a particle trajectory tracking model for particle interactions with the cell surface. The integrated model can be used to predict the behavior of nanoparticle transport in tissues for a variety of infusion parameters.

2.1 Fluid Flow and Tissue Deformation during an Infusion Process

We assumed that the porous structure before an injection is homogenous. The nanofluid with a particle volumetric concentration less than 5% is considered as an incompressible dilute colloidal fluid where the presence of the particles does not significantly affect the transport properties of the fluid [62]. The effects of gravity, osmotic effects, particle agglomeration on fluid transport, and fluid exchange between the interstitial fluid and blood or lymph vessels are not considered in this study [7, 34]. Fluid flow and tissue deformation are considered steady state [54]. With these assumptions, the fluid flow through tissue is described by Darcy's equation [25]

$$\nabla \cdot (\varepsilon \mathbf{v}) = 0 \qquad (1)$$

$$\nabla p_f = -\frac{\varepsilon \mu}{K} \mathbf{v} \ , \qquad (2)$$

where ε is porosity, $\mathbf{v}$ is interstitial fluid velocity vector, p_f is fluid pressure, μ is the viscosity of the fluid, and K is permeability of the tissue.

During an infusion, backflow forms as the hydraulic pressure opens an annular space surrounding the needle outer surface. The bulk fluid flow in the annular space is governed by the conservation of mass and momentum, which are

$$\nabla \cdot \mathbf{v} = 0$$

$$\mathbf{v} \cdot \nabla \mathbf{v} = -\frac{1}{\rho} \nabla p_f + \frac{\mu}{\rho} \nabla^2 \mathbf{v} \qquad . \qquad (3)$$

In the poroelastic model, the solid phase of the medium is assumed to be Hookian material, incompressible, isotropic, and fully saturated with fluid. The deformation during the infusion is infinitesimal. Also, the study focuses on the resultant deformation rather than the deforming process, i.e., the deformation is instantaneous. The constitutive equation for tissue deformation yields:

$$G\nabla^2 \mathbf{u} + (\lambda + G)\nabla(\nabla \cdot \mathbf{u}) = \nabla(\varepsilon p_f), \qquad (4)$$

where $\mathbf{u}$ is the displacement vector, and G and λ are the Lamé constants. Given Young's module and Poisson ratio, G and λ can be calculated by using the following two relationships *λ=Ev/((1+v)(1-2v)) and G=E/(2(1+ λ))*.

One should note that the porosity and permeability in Eqs. (1) and (2) are spatially varying in the presence of tissue deformation; both are functions of dilatation e, where $e = \nabla \cdot \mathbf{u}$. With the assumption that the volume of the solid phase of the porous medium

does not change for small deformation, the porosity ε is calculated by the following expression [7, 8],

$$\varepsilon = \frac{\varepsilon_0 + e}{1 + e}, \tag{5}$$

where ε_0 is the tissue porosity in the absence of deformation. Various empirical relationships have been proposed to quantify permeability K as a function of dilatation e [15, 19, 28]. In this study, we employed a commonly used relation proposed by Lai and Mow [28] which yields an exponential increase in tissue permeability with dilatation e:

$$K = K_0 \exp(Me), \tag{6}$$

where K_0 is the permeability in the absence of deformation and M is a material constant that governs the variation of permeability with the dilatation. Typically it is related to the tissue properties, the densities of the cells, and the extracellular matrix [7]. Through curve-fitting of experimental data, previous studies suggest that M is in the range from 0 to 5 [7, 28, 53]. We used a constant $M=2$ in this study.

2.2 Nanoparticle Convection and Diffusion in Tumor

The transport of large therapeutic agents in tissue is typically described by convection and diffusion equations with extra terms to consider mechanisms such as internalization of drugs by cells, collection of macromolecules by circulation, reactions on the cell surfaces, etc. In this study, the short injection duration (less than one hour) renders the extravascular exchange of nanoparticles through a capillary wall insignificant. The nanoparticle internalization does not alter the macroscale particle concentration profile, and thereby, can be neglected. The binding of nanoparticles on the cellular structure, on the other hand, is an important mechanism that reduces the particle concentration in the fluid phase and substantially affects the nanoparticle distribution in the tissue [37, 54]. The attachment of nanoparticles to the cellular structure can be treated as a concentration-dependent reaction that consumes particles in the fluid phase [58]. This phenomenon can be described by a volumetric deposition rate in the convection and diffusion equation. Deposition rate coefficient, a quantity analogous to the rate constant of a chemical reaction, is used to quantify the dependence of the volumetric deposition rate of the particles on local particle concentration, particle size and properties, local velocity, porous structure, etc. With the assumption that the particle binding to the cell surfaces is irreversible, the modified equation for nanoparticle transport in a porous tissue is

$$\frac{\partial C}{\partial t} + \nabla \cdot (\mathbf{v}C) = \nabla \cdot [D_e \nabla C] - k_f C, \tag{7}$$

where C is the molar concentration of the particles in the fluid, the term $k_f C$ represents the volumetric deposition rate of the particles on the solid phase, and k_f is the deposition rate coefficient. D_e is the effective diffusion coefficient which is calculated based on the diffusion coefficient in an unbounded liquid phase and tortuosity of the tissue [14]:

$$D_e = D_0 \frac{L}{F\tau(\varepsilon)}, \qquad \text{and} \qquad D_0 = \frac{k_B T}{3\pi\mu d_p}, \tag{8}$$

6

where D_0 is the diffusion coefficient in an unbounded liquid phase, k_B is the Boltzmann's constant, T is the absolute temperature, d_p is the particle diameter, L is the factor responsible for hydrodynamic reduction of the diffusion coefficient in the pore, $\tau(\varepsilon)$ is the tortuosity which is the function of porosity ε, and F is a shape factor valued from one to four [44, 51]. The volumetric concentration of the nanoparticles bounded to the solid structure S can be calculated by the equation

$$\frac{\partial S}{\partial t} = k_f C . \tag{9}$$

2.3 Particle Trajectory Tracking Model for Calculation of k_f

The deposition rate coefficient is a function of many factors such as local fluid velocity, geometry of the porous structure, the surface properties of both particle and the solid, etc. k_f can be determined by experimental measurement and theoretical calculation in the studies of colloidal particle transport in sand or soil bank [58, 59]. When experimental measurement is not available or feasible, particle trajectory tracking method is widely used to determine the deposition rate coefficient [40]. In this method, the suspended particles are treated as individual entities and the trajectories of these particles in a representative unit structural cell of a porous medium are determined based on the forces acting on these particles under a set of conditions. When a particle is in contact with the solid surface, a binding is counted [38]. By delivering a large amount of particles into the unit structural cell, the collector efficiency η_s, defined as the ratio of the particles captured by the solid surface to those brought into a unit structural cell of the porous medium, can be determined. η_s measures the probability of particle interception by the solid structure. Once the collector efficiency is calculated, the deposition rate coefficient for a porous medium consisting of spherical bodies with a diameter of d_c, can be calculated by the equation [58]:

$$k_f = \frac{3(1-\varepsilon)}{2\varepsilon d_c} \eta_s |\mathbf{v}| , \tag{10}$$

where $|\mathbf{v}|$ is the magnitude of the local fluid velocity.

Happel's sphere-in-cell model [16] is widely used as the unit structural cell for granular porous media [38, 43, 59]. As schematically shown in Fig. 1, it consists of a solid spherical body representing a cell and a uniform layer of fluid that envelops the sphere. The thickness of the fluid layer is calculated as $\gamma = a_c[(1-\varepsilon)^{-1/3} - 1]/2$, where a_c is the diameter of the solid sphere [38]. Selection of unit structural cell for tissue is a challenge due to the existence of the extracellular matrix. While tissues are typically conceptualized as porous structures consisting of nearly spherical cells in the studies of drug delivery [8], Netti et al. [39] reported that collagen can significantly hinder the diffusion of large molecules. However, it is unclear to what extent the extracellular matrix affects the convective transport of the particles due to limited study on this topic. Further, it is a formidable task to include the collagen fibers in a unit cell at current stage. Considering that the focus of the study is the effect of particle deposition on particle transport, we

7

study an ideal situation where the presence of the extracellular matrix can be neglected and use the Happel's model as the unit structural cell for tissue.
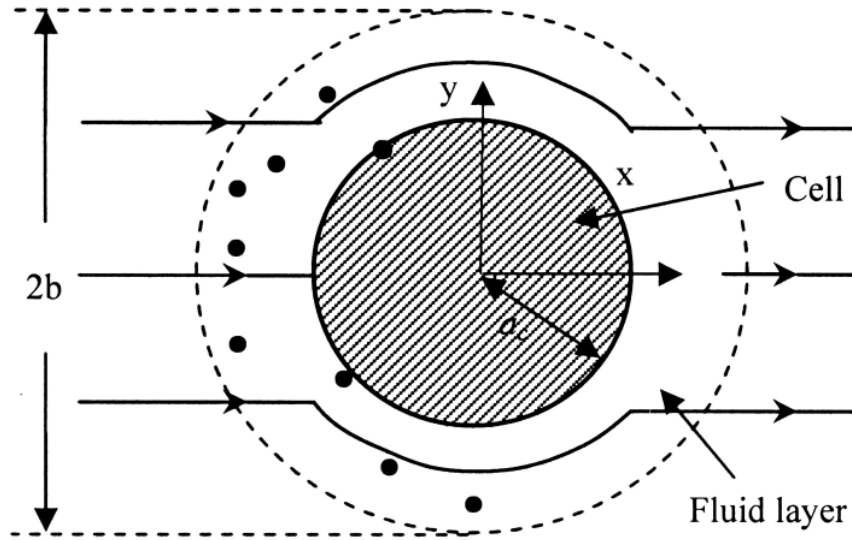
Figure 1 Happel's sphere-in-cell for the particle trajectory tracking analysis, $b = a_c(1 - \varepsilon)^{-1/3}$, where ε is porous porosity. Black dots refer to nanoparticles [38]

The details of the particle tracking model can be found in the literature [54]. In brief, we assume that the particles are small (nanosized particles), spherical, chemically inert, solid, and very dilute in a liquid that flows with a low *Re* number in the laminar regime. Hydrodynamic interactions among the particles are neglected. Typically the particles are properly coated to prevent agglomeration.

The forces that act on a particle near a solid surface immersed in the moving fluid include van der Waals attractive force, electrostatic double layer force, hydrodynamic drag force, lift force, buoyancy force, and Brownian motion. The van der Waals force and electrostatic double layer force act along the normal direction of a surface and only become significant at close separation distance between the particles and a surface. The lift force pushes particles away from the surface towards the direction of increasing velocity [24, 31]. A particle fully immersed in a fluid also experiences an upward buoyancy force. For a nanoparticle, buoyancy force is insignificant when compared with other forces due to its small size. Basset force which is important for a particle accelerated at a high rate is neglected due to the laminar flow conditions used in the current study [24]. Magus force is considered negligibly small when compared to the drag force because of the small particle size [24].

For submicron-sized colloids whose relaxation time is small, one could neglect the inertia force and assume that the particles relax to the fluid velocity instantaneously. The colloidal particle trajectory is then governed by the Stochastic Langevin equation [30, 38, 61]:

$$dr_j = (\frac{D}{k_B T}\sum_i \mathbf{F}_i + \mathbf{v})\Delta t + (\Delta \mathbf{r})_j^B, \qquad (11)$$

where dr_j is the displacement vector of j_{th} particle, D is the particle diffusivity, $\mathbf{F}_i$ represents the forces acting on the particle, $\mathbf{v}$ is the fluid velocity, and $(\Delta \mathbf{r})_j^B$ is the random Brownian displacement. Δt is the time interval used in the integration.

The velocity expressions in a Happel's sphere-in-cell shown in Fig. 1 are obtained directly from the stream function of Stokes flow in the Happel's model. The radial and azimuthal velocities, respectively, are [16]

$$v_{f,r} = -V_\infty \cos\theta(\frac{K_1}{r*^3} + \frac{K_2}{r*} + K_3 + K_4 r*^2), \quad \text{and}$$

$$v_{f,\theta} = \frac{1}{2}V_\infty \sin\theta(-\frac{K_1}{r*^3} + \frac{K_2}{r*} + 2K_3 + 4K_4 r*^2), \qquad (12)$$

where $K_1=1/w$, $K_2=-(3+2p^5)/w$, $K_3=(2+3p^5)/w$, $K_4=-p^5/w$, $w=2-3p+3p^5-2p^6$, $p=(1-\varepsilon)^{1/3}$, and $r*=2r/d_c$.

When a freely moving particle travels near a rigid surface, the extra viscous resistance exerted by the wall and the rotation of the particle can substantially modify both the velocity and mobility of the particle. This is referred to as hydrodynamic retardation. The correction factors used in this study are given in the reference [54].

Viscous Lift Force
Particles traveling across a velocity gradient caused by the presence of a wall can experience a lift force that directs a particle away from the wall. Saffman force is insignificant for nanoparticles having a very small Stokes number [47]; rather, pressure difference across the particle and particle rotation can cause an appreciable lift force on a non-inertia particle [31]. Cox and Hsu derived the following expression to calculate the lift velocity for non-inertia spherical particles in a laminar parabolic flow field near a single vertical plane [10]:

$$\mathbf{v}_{lift} = \frac{55}{144}\frac{\rho d_p v_{f,\max}^2}{2\mu}\left(\frac{d_p}{2h_{\max}}\right)^2\left(1-\frac{h}{h_{\max}}\right)\left(1-\frac{73}{22}\frac{h}{h_{\max}}\right), \qquad (13)$$

where h is the distance between the particle centre and the wall, h_{max} is the distance at which the velocity profile reaches its maximum $v_{f,max}$. More details about the calculation of the lift force can be found in the reference [1]. Given the lift velocity $\mathbf{v}_{lift}$, the lift force can be obtained accordingly:

$$\mathbf{F}_{lift} = 3\pi\mu d_p \mathbf{v}_{lift}. \qquad (14)$$

van der Waals Force and Electrostatic Double Layer Force
The potential for particle-surface interactions within the interaction range is calculated according to the Derjaguin, Landau, Verwey and Overbeek (DLVO) theory [46]. The DLVO potential interaction forces can be derived through the differentiation of the potential interaction energies [20]:

$$\mathbf{F}_{potential} = -\frac{\partial}{\partial h}(A_{elec} + A_{vdW}), \tag{15}$$

where A_{elec} is the potential due to electrostatic interaction and A_{vdW} is the potential due to van der Waals force between particles and a surface. Since the size of a nanoparticle is much smaller than that of a cell, their interactions can be approximated as those between a particle and a flat wall.

The van der Waals interaction energy between a sphere and a wall at a distance of h is expressed as [20]:

$$A_{vdW} = -A_H d_p /(12h), \tag{16}$$

where A_H is the Hamaker constant, which can be calculated by an empirical formulation provided by the reference [46].

According to the Gouy-Chapmann model of a diffuse double layer and electrostatic Poisson-Boltzmann equation, A_{elec} between a spherical particle and a flat surface with the zeta-potentials of ψ_1 and ψ_2, respectively, is given by the following equation:

$$A_{elec} = 64\pi\varepsilon_r\varepsilon_0 (\frac{k_B T}{zE})^2 \frac{d_p}{2} \times [\tanh(\frac{zE\psi_1}{4k_B T})\tanh(\frac{zE\psi_2}{4k_B T})]e^{-\kappa h}, \tag{17}$$

where ε_0 is the vacuum permittivity, ε_r is the relative dielectric constant of the water, I is the electron charge, and θ is the valence of the electrolyte. The effect of the aqueous environment is reflected by the Debye-Hückel parameter κ.

Brownian Motion
Brownian motion is formulated through Brownian displacement $(\Delta\mathbf{r})^B$, a random value taken from a Gaussian white noise distribution with a zero mean $W(t)$ and a specific intensity that relates to the Mean Square Displacement (*MSD*). Stokes-Einstein equation is used to calculate the *MSD* [20]:

$$MSD^2(t) = \left\langle(\Delta\mathbf{r})^2\right\rangle = \frac{2k_B T}{f}|\Delta t| = 2D|\Delta t|, \ f = 3\pi\mu d_p \tag{18}$$

A freely moving particle may experience rotations near a solid surface. In the case of spheroid and ellipsoidal particles, the determination of the rotational velocity is essential because the interaction energy is dependent on the particle orientation. However, spherical particles are symmetric and hence are less likely to be affected by the particle rotation [61]. Therefore, the particle rotational velocities are neglected in the trajectory tracking analysis. The effect of particle rotation on the motion of a particle near a surface is considered through the lift force and corrections of the fluid velocity and particle mobility.

The particle trajectories are determined by integrating Eq. (11) using the predictor-corrector method [27]. At the beginning of a particle trajectory analysis, a large number of particles are distributed randomly over the curved segment extending from $y=0$ to $y=b$ as shown in Fig. 1 [45]. The vertical position of a particle is determined by

$$y_0 = \xi_i b \, , \tag{19}$$

where ξ_i is a sequence of uniformly distributed random number in the range of zero to unit, and b is the radius of the fluid shell shown in Fig. 1. Once its vertical position is determined, the x coordinate of an entering particle can be determined as

$$x_0 = -(b^2 - y_0^2)^{1/2} \, . \tag{20}$$

A particle deposition is counted if the calculated trajectory of a particle reaches the solid surface. Through calculating the trajectories of a number of particles, the collector efficiency can be determined for various combinations of parameters such as particle size, surface properties, local fluid velocity, etc. Note that the number of particles used in the simulation should be sufficiently large to ensure that the collector efficiency is independent of the particle number and the result is statistically meaningful.

The time step Δt should be sufficiently small such that the deterministic forces remain constant during each time interval. Also, the assumption of negligible particle inertia requires that the time step should be much greater than the particle relaxation time $\tau_p = m_p f^{-1}$. Thus, the requirement of the time step may be written as $\tau_p \ll \Delta t \ll \tau_u$ where τ_u is the time increment at which deterministic velocity is considered constant. This study used a Δt of 10^{-5} s.

2.4 Model integration

The three components of the model were integrated to simulate nanofluid transport during an infusion process by conducting the following tasks in sequence: (a) Equations (1) – (6) were solved iteratively to determine the fluid velocity field, tissue deformation, and the distribution of the porosity. This provided information on the range of velocity and porosity for a given set of infusion conditions; (b) the particle trajectory tracking was conducted to calculate the deposition rate coefficients for various velocities and tissue porosities in the range prescribed in step (a). We used curving fitting to derive the relationship of deposition rate coefficient to velocity and porosity; (c) Equation (7) for nanoparticle convection, diffusion, and deposition in the tissue can be solved with velocity field obtained in the previous calculation. The dependence of particle deposition on velocity and porosity is accounted for by using the function obtained in step (b). Since Eq. (7) is transient, the injection duration is determined by injection amount and injection rate. The geometries and the boundary conditions used in the simulations are given in section 4 and 5. A commercially available multiphysics software COMSOL® was used in this study. Major simulation parameters, tissue and particle properties are given in Table 1.

Table 1. Major parameters and properties in the simulation

Properties and Parameters	Values
Infusion amount	0.1 cc
Needle size	22, 26, and 32-gauge, Hamilton needle
Infusion rate	5 ~15 μl/min
Nanofluid concentration	0.75M ferrofluid (3% by volume)
Magnetic nanoparticle	Fe_3O_4

Nanoparticle density	5240 kg m^{-3}
Nanoparticle diameter	20 nm
Nanoparticle diffusivity	10^{-11}~10^{-12} m^2 s^{-1} [54]
Nanoparticle surface zeta potential	–20 mV ~ – 60 mV
Tumor diameter	10 mm
Young's module of tissue (E)	60 KPa [9]
Young's module of tumor (E)	0.2 ~ 0.5 MPa [4,7]
Tumor Permeability	5×10^{-16} m^2 [7, 39]
Tissue permeability	1×10^{-14} m^2 [57]
Tissue/Tumor Poisson ratio	0.35 [7, 34]
Tissue Porosity	0.4 [34]
Tumor porosity	0.2 [39]
Cell diameter	20 μm
Cell surface zeta potential	–20 mV [54]

3.   PREDICTION OF DEPOSITION RATE COEFFICIENT

In this study, the dependence of the deposition rate coefficient on particle surface charge and porosity at various velocities was studied using the particle trajectory tracking model. Shown in Fig. 2a are the variations of the deposition rate coefficient (k_f) with fluid velocity for particles with different surface charges: –20, –40 and –60 mV. Nanoparticles of 20 nm diameter, cells of 20 μm diameter, and tissue porosity of 0.2 were used in this simulation. The result shows that deposition rate coefficient decreases with local fluid velocity monotonously for all the surface charges. Due to the repulsive force that keeps particle away from the cell surface, increasing the surface charge of the particles can significantly reduce the deposition rate coefficient. Figure 2b shows the dependence of deposition rate coefficient on local velocity for three tissue porosities: 0.2, 0.3 and 0.4. There is clear indication that porosity is an important parameter than affects the rate of particle deposition on the cell surface. A higher porosity leads to lower deposition coefficients because of the larger interstitial space between the cells.
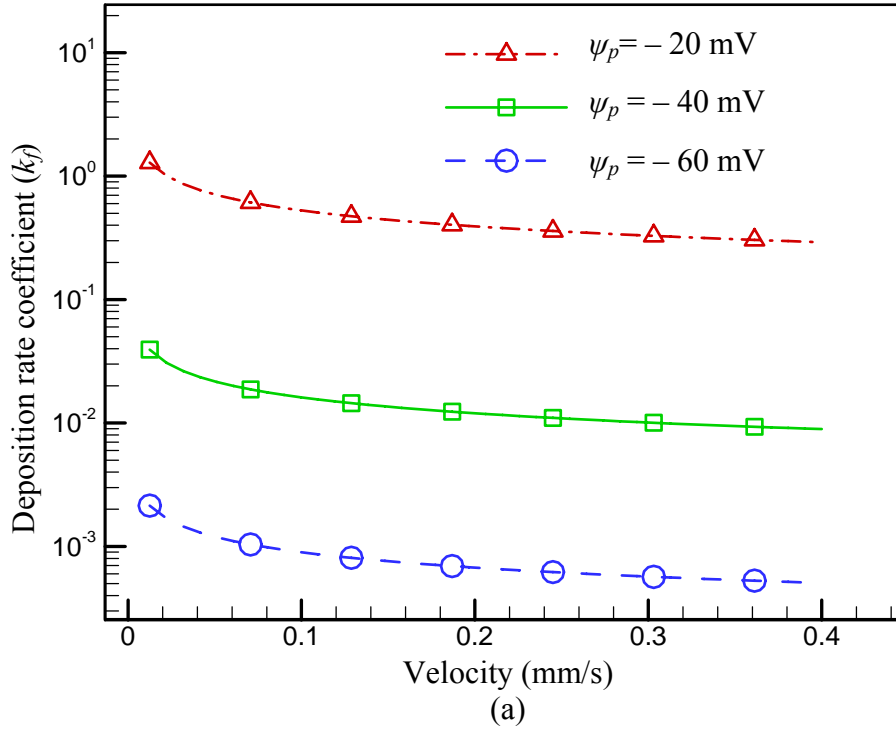
Figure 2a Variations of deposition rate coefficient (k_f) with velocity for various surface charges of the particles ($\psi_c = -20$ mV, d_p=20 nm, a_c=20 μm, ε=0.2)
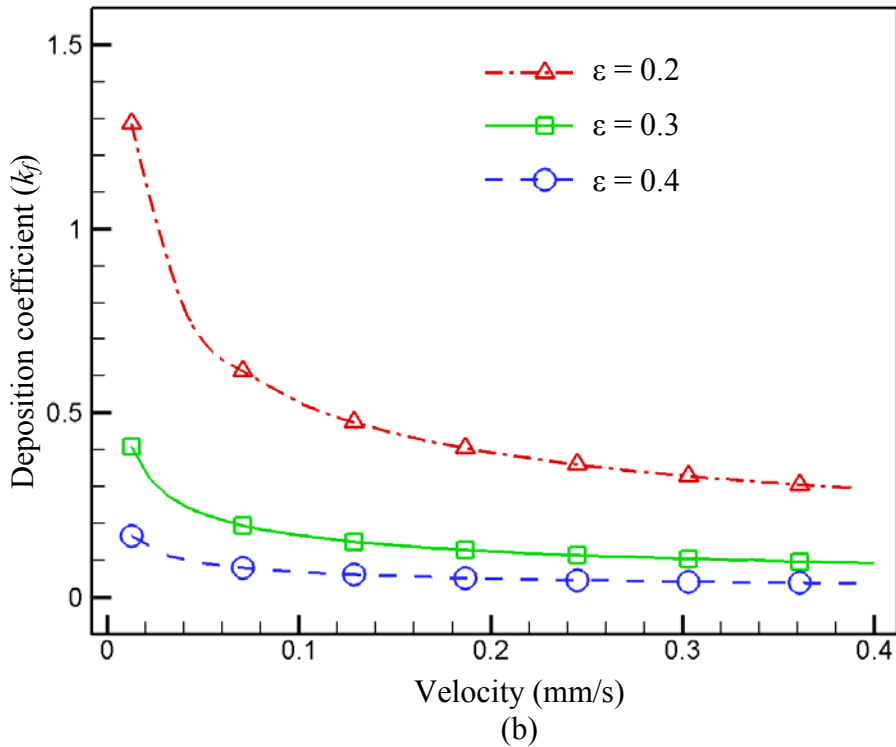
Figure 2b Variations of the deposition rate coefficient (k_f) with velocity for various porosities, ($\psi_c = -20$ mV, $\psi_p = -20$ mV, d_p=20 nm, a_c=20 μm)

4. ONE DIMENSIONAL NANOPARTICLE DISTRIBTIONS IN NON-DEFORMABLE TUMORS

The multiscale model was used to calculate one-dimensional particle distribution in a non-deformable spherical tumor of 10 mm diameter for various infusion rates, particle surface charges, and tissue porosities. Nanofluid is assumed to be delivered from a point source at the center of a tumor. The boundary conditions at the center of the tumor are constant infusion velocity and nanoparticle concentration. At the tumor outer boundary, $p=0$ and $\partial C / \partial r = 0$ are applied. Figure 3 shows the particle distributions along the radial direction for various infusion rates. It is observed that the total particle concentration decreases exponentially in the radial direction at the center. The particle concentration distributions for various surface charges and tissue porosities at the infusion rate of 5μl/min are shown in Figs. 4 and 5, respectively. It is evident that nanoparticle surface potential plays a vital role in the infiltratoin of the nanoparticles in tumors. Consistent with the relationship between deposition rate coefficient and tissue porosity demonstrated in Fig. 2b, nanoparticle distribution is sensitive to the change in tissue porosity.
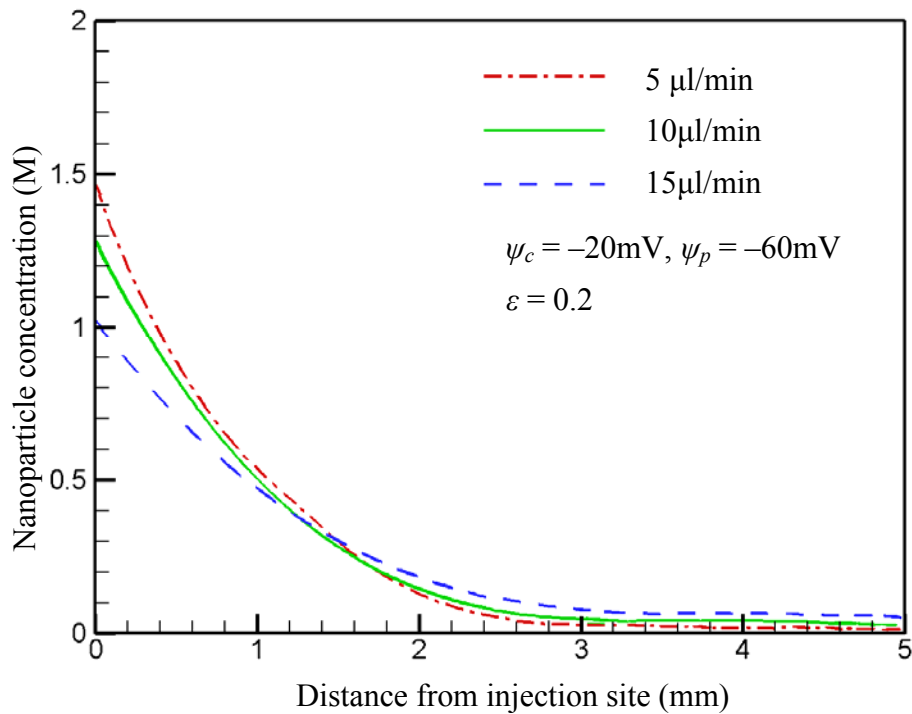
Figure 3 Distributions of nanoparticle concentration for various injection rates.
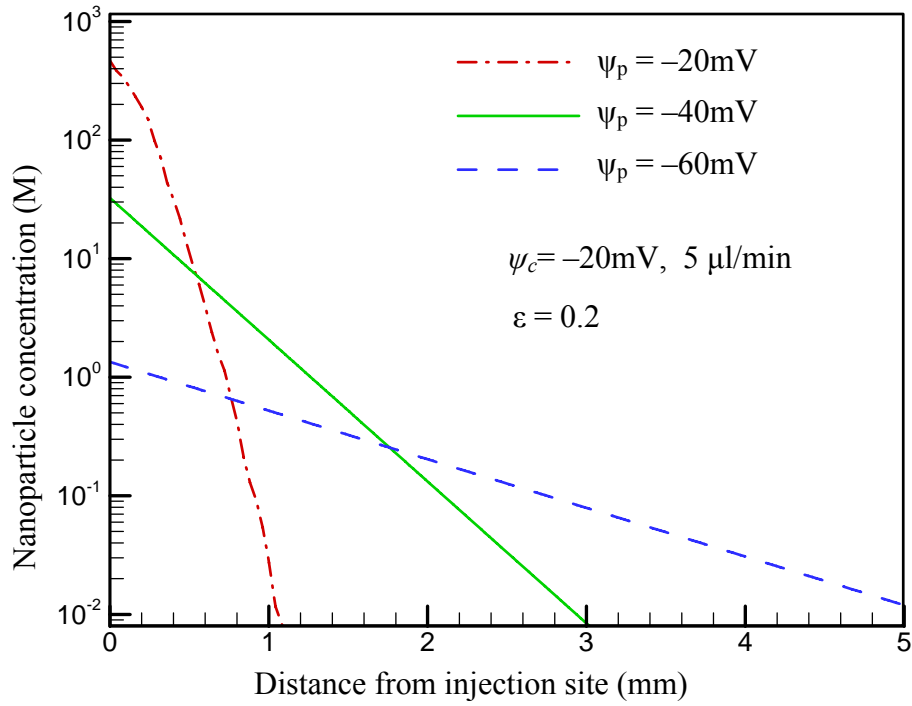
Figure 4 Distributions of nanoparticle concentration for various particle surface charges
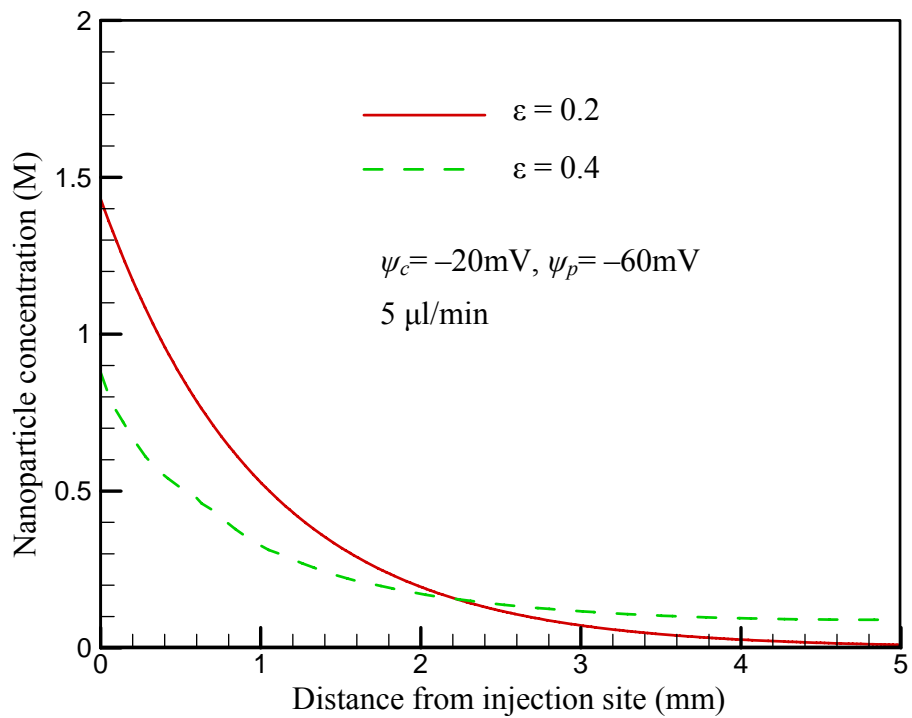
Figure 5 Distributions of nanoparticle concentration for various tumor porosities.

5.   NANOFLUID INFUSION IN DEFORMABLE TUMORS

We studied the nanofluid infusion process in deformable tissues in an axisymmetric domain depicted in Fig. 6. It schematically shows a nanofluid infused through a needle into a spherical tumor embedded in 20 mm thick normal tissue. The boundary conditions used in this study are as follows: a finite pressure P_{inf} and constant concentration of the nanofluid $C=C_0$ are applied at the needle tip; at the outer boundary $r=R$, $P=0$, and $\partial C / \partial \mathbf{n} = 0$, where $\mathbf{n}$ is the unit normal vector at the outer boundary. The value of P_{inf} is adjusted in the simulation so that it yields the desired infusion rate. No-slip condition is applied on the surfaces of tissue and the needle exposed to the backflow. For tissue deformation, a constant hydraulic pressure P_{inf} is applied on the needle tip, which yields

$$(2G+\lambda)\frac{\partial u_z}{\partial z} = -P_{\text{inf}} . \tag{21}$$

At $r=R$, we consider a case of deep-seated tumor and a fixed boundary condition, $\mathbf{u}=0$ is applied. The interface between the tissue and needle is considered deformable interface which allows the tissue to recede from the needle surface. The original tumor porosity is 0.2 and the surface charge of the particle is –60 mV. The nanofluid concentration, tumor size, tumor and tissue properties, and other major parameters used in the model are given in Table 1.
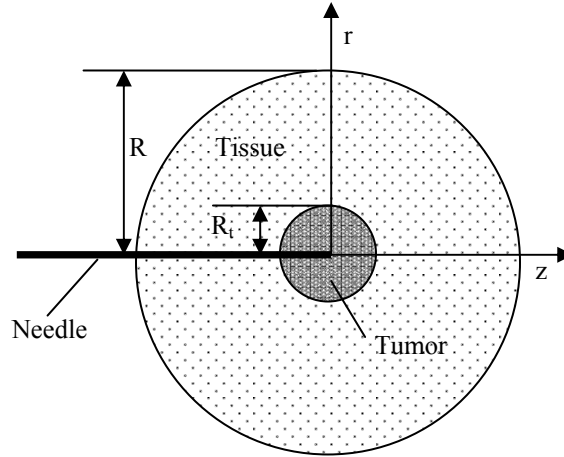
Figure 6 Configuration for nanofluid infusion in a tumor embedded in 20 mm normal tissue.

Shown in Fig. 7a is the nanoparticle distribution in a tumor for a baseline case where the infusion rate is 5 µl/min, the needle size is 26 gauge, and the Young's modulus E is 0.5 MPa. It can be seen that the particle distribution is not spherically symmetric; rather, it illustrates particle transport along the needle track due to the formation of backflow. The backflow length is 6 mm. Figure 8a shows the corresponding porosity distribution in the tumor. Increased porosity near the needle tip is observed. A similarity between the shapes of the concentration and porosity distributions is observed, suggesting the influence of enlarged tissue porosity on the particle dispersion.
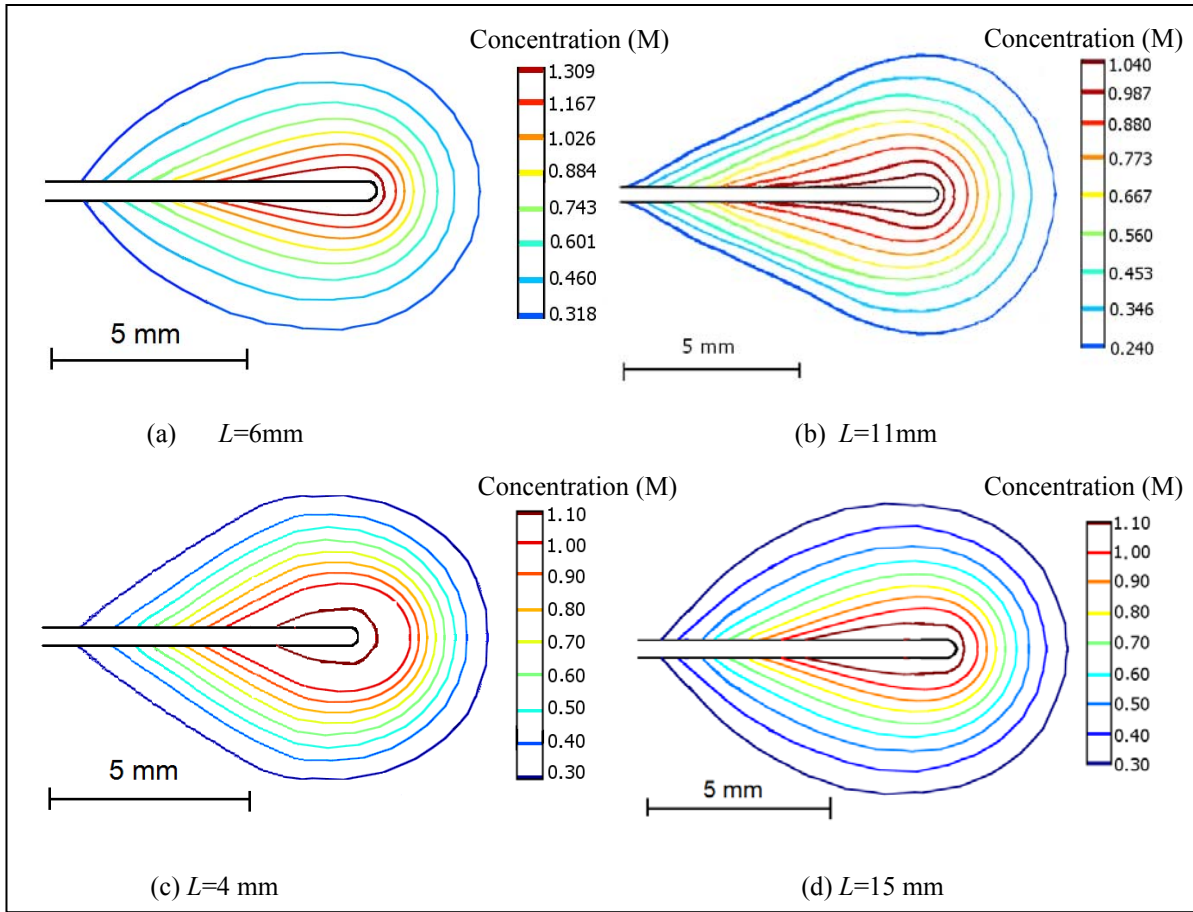
Figure 7 Distributions of nanoparticle concentration for (a) baseline case with infusion rate of 5µl/min, E=0.5MPa, and 26 gauge needle, (b) 10 µl/min, (c) 32 gauge needle, and (d) E=0.2 MPa. L is the backflow length.
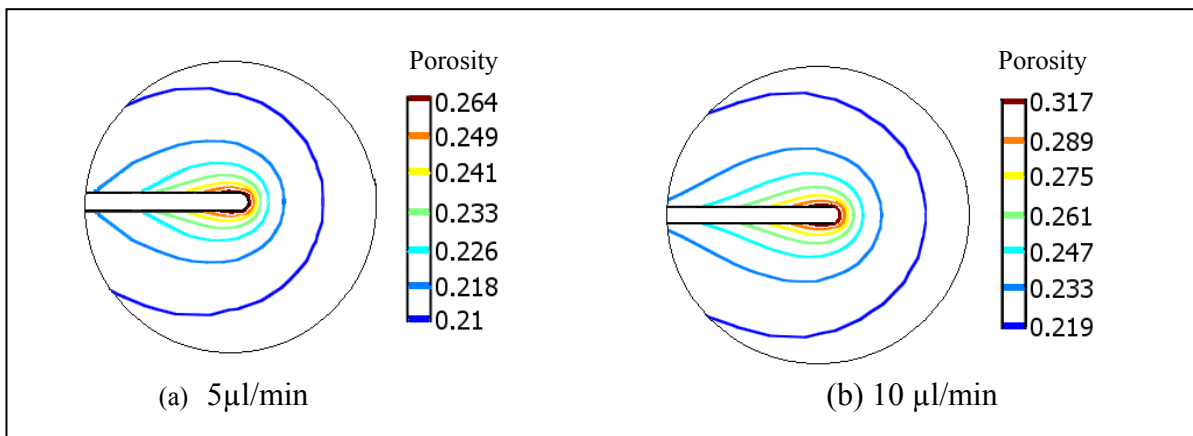
Figure 8 Distributions of tissue porosity for the infusion rates of (a) 5µl/min, and (b) 10 µl/min. (E=0.5MPa, ε_0=0.2, M=2, 26 gauge needle)

The effect of the infusion rate on tissue deformation and particle distribution is studied by changing the infusion rate while holding other parameters prescribed in the baseline case constant. Shown in Figs. 7b and 8b, respectively, are the particle and porosity distributions for the infusion rate of 10 µl/min. In addition to a longer backflow length, the infusion rate of 10 µl/min yields a larger tissue porosity and lower particle concentration near the injection site. The variations of porosity and nanoparticle concentration along the injection direction for different infusion rates are shown in Figs. 9a and 9b respectively. For both infusion rates, tissue porosity and nanoparticle concentration decrease monotonously in the radial direction from the injection site. A higher infusion rate causes a deeper particle penetration depth and lower nanoparticle concentration at the needle tip. In comparison to the particle distribution in the absence of tissue deformation (Figure 3), the particle concentration decays less sharply in the radial direction.

A 32 gauge needle was employed in the simulation to examine the effect of the needle size on the nanofluid infusion. Note that 32 gauge needle is thinner than a 26 gauge. The predicted distribution of nanoparticles is shown in Figure 7c. It demonstrates that reducing the needle size yields a shorter backflow length (4 mm) despite of the elevated infusion pressure required for delivering the same amount of infusate. This result is consistent with the study of Morrison, et al. [36]. Figures 10a and 10b compare the variations of the porosity and particle concentration along the injection direction, respectively, for two different needle sizes, 26 and 32 gauge. There is clear indication that the smaller needle size is associated with a larger tissue pore size, and a lower particle concentration at the needle tip. Also, a deeper penetration depth occurs when the smaller needle size is used.

Figure 7d displays the nanoparticle distribution for tumors with a different value of Young's modulus, E=0.2 MPa. In comparison to Figure 7a where E=0.5 MPa, a lower value of Young's Modulus makes the tissue easier to deform, leading to elongated backflow length and enlarged porosity near the needle tip (Figure 11a). As a result, there is less particle accumulated near the needle tip (Figure 11b).
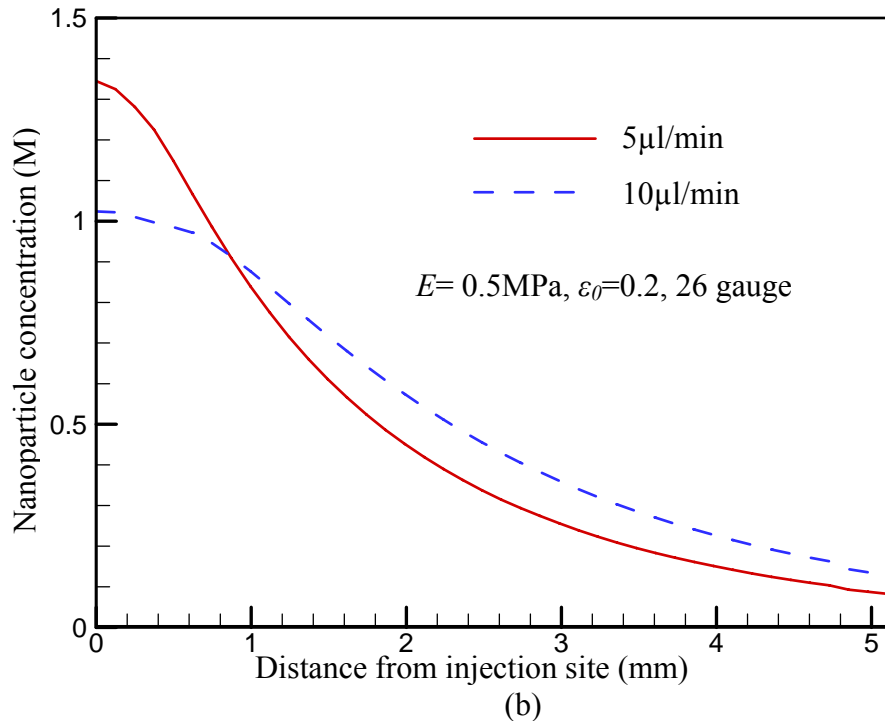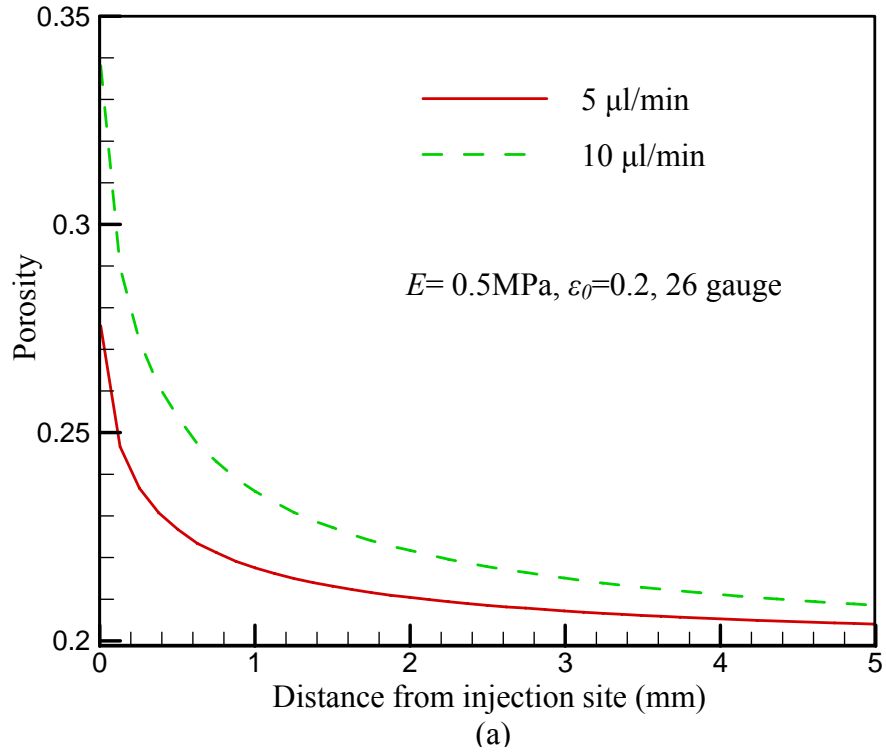
Figure 9 Variations of porosity (a) and particle distribution (b) along the injection direction for various infusion rates (E=0.5MPa, ε_0=0.2, M=2, 26 gauge needle)

(a)

(b)
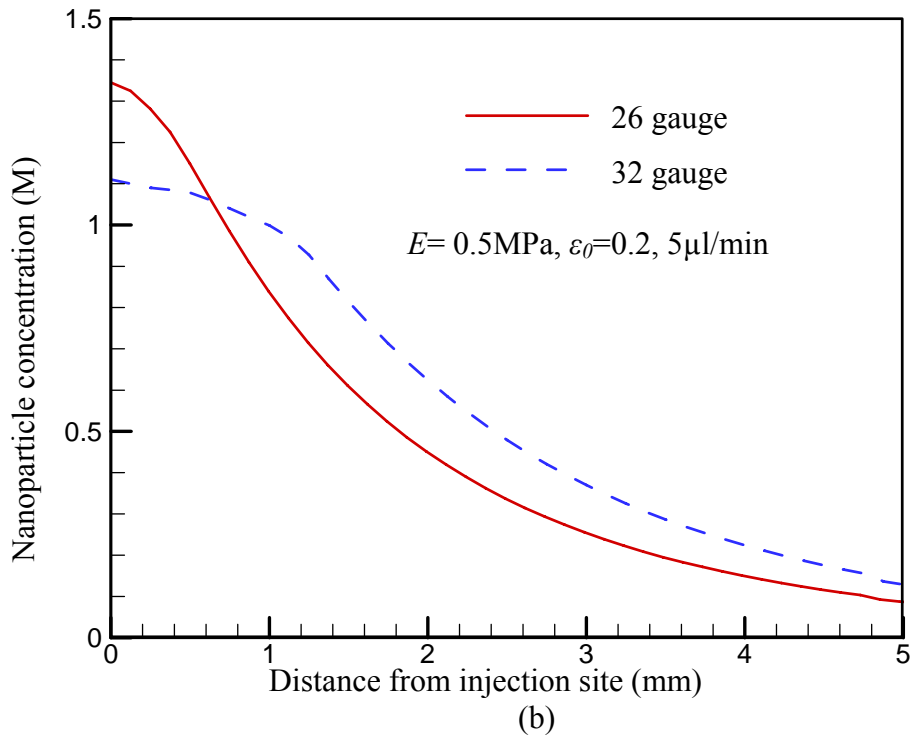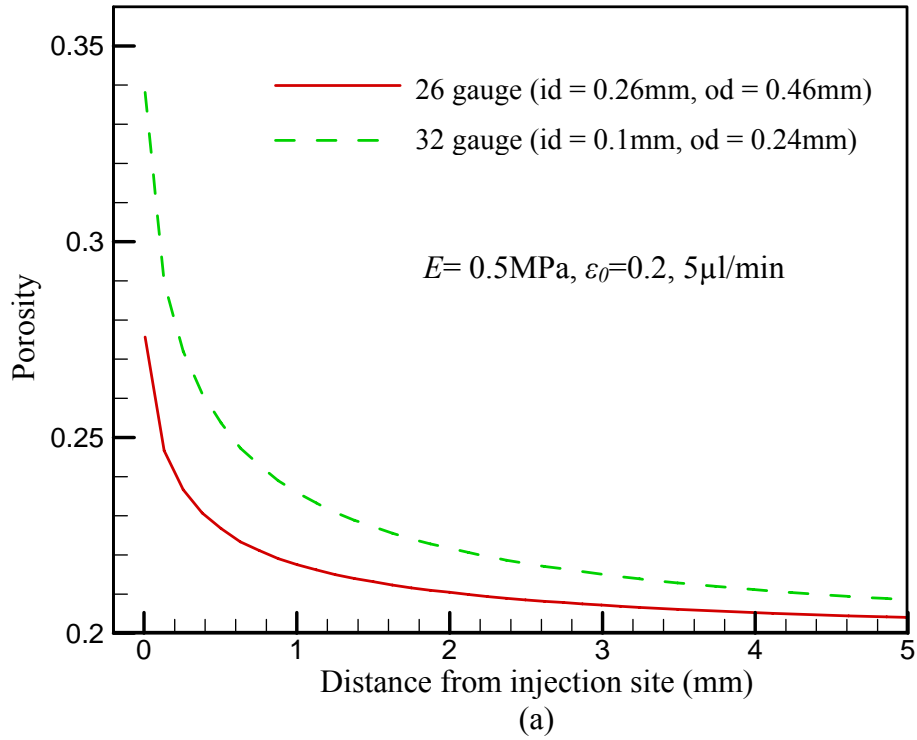
Figure 10 Variations of porosity (a) and concentration (b) along the injection direction for various needle sizes.

(a)

(b)
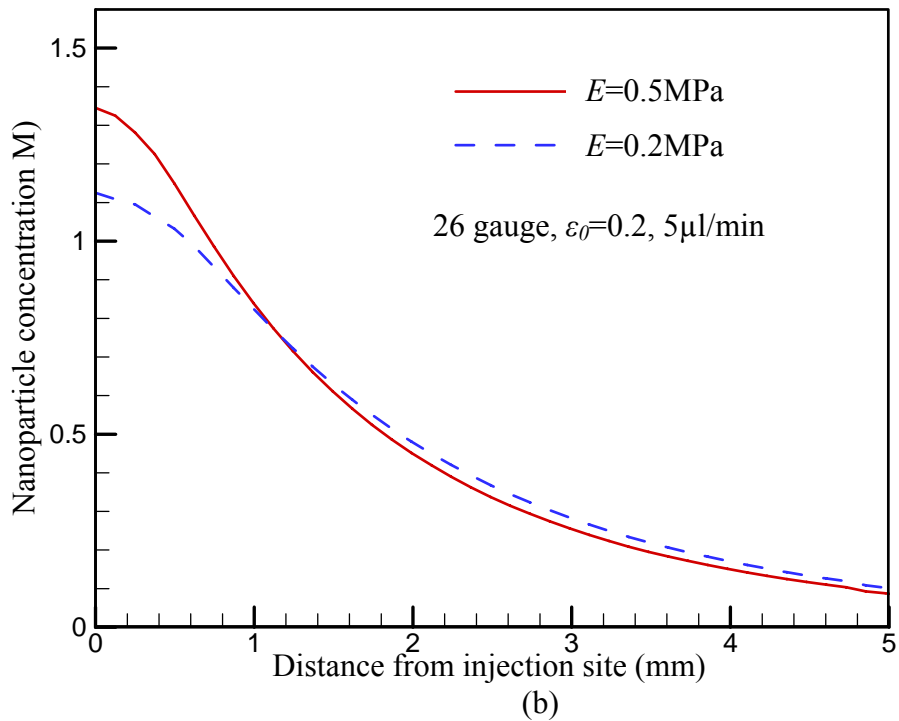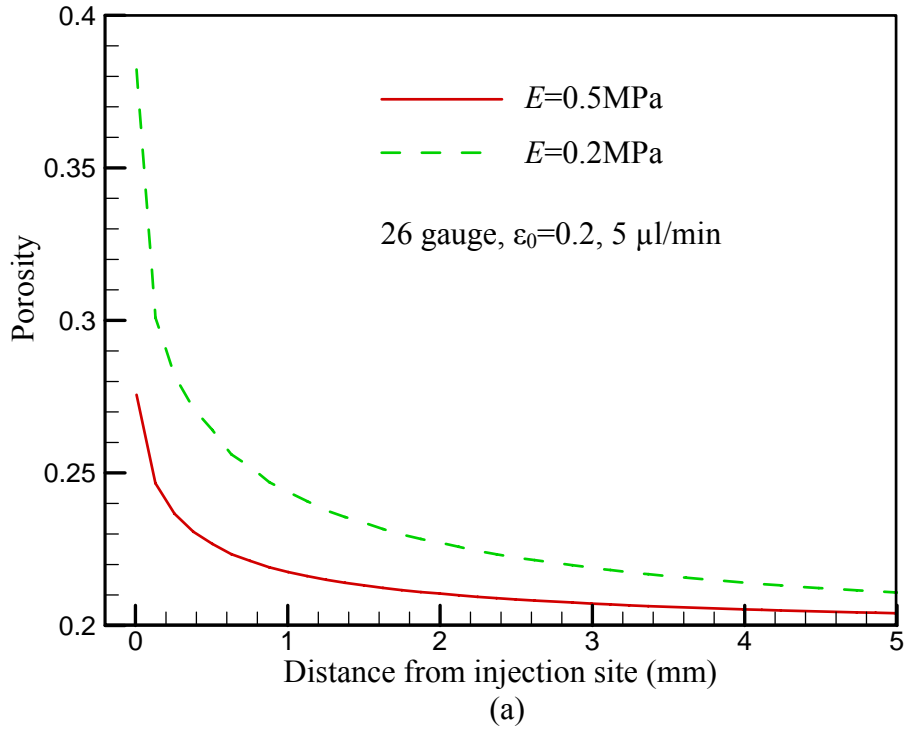
Figure 11 Variations of (a) porosity and (b) particle concentration along the infusion direction for various Young's moduli.

We compared the nanoparticle concentration distributions in a tumor with various amounts of nanofluid infused. The pattern of nanoparticle distribution in a tumor with

0.2cc nanofluid is similar to that shown in Fig. 7a and therefore, is not displayed. The variations of nanoparticle distributions along the injection direction are shown in Figure 12.
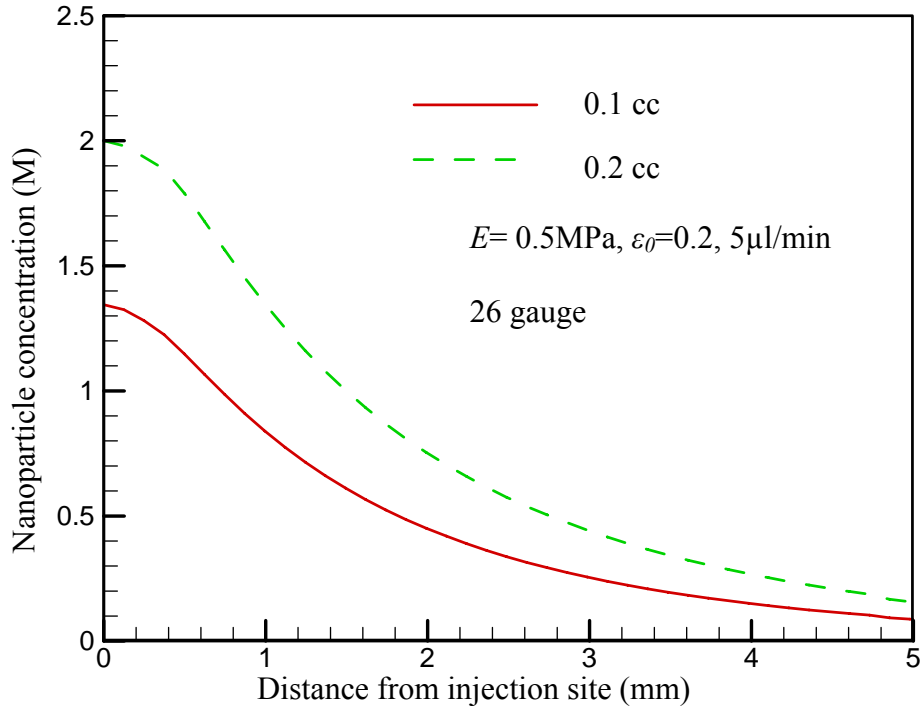
Figure 12 Variations of particle concentration distribution along the injection direction for various injection amounts.

6. DISCUSSIONS

In hyperthermia treatment of cancer, tumor cells are killed by maintaining sufficient temperature elevations for a period of time. Typically, 43°C (6°C above 37°C) is the minimal temperature threshold to induce cytotoxic responses if the heating time is longer than one or two hours. Salloum et al. [50] proposed an optimization algorithm for irregular large-sized tumors with magnetic nanoparticles being delivered at multiple sites. The developed algorithm allows adjustments of injection parameters such as injection sites, injection rates and injection amounts for elevating at least 90% of a tumor above certain threshold temperature (43°C), while less than 10% of the normal tissue temperatures exceed this threshold. The success of this optimization algorithm requires controlled particle distribution at each injection site. Understanding the particle transport mechanism and the effects of injection parameters are critical for designing the multisite injection strategy.

Particle binding to the cellular structure has been identified as an important factor that causes the non-uniform particle distribution in tissues and limits the penetration depth of the particles after infusion [54]. The rate of particle binding to the cell surface is dependent on many factors, among which we consider the interstitial fluid velocity, porosity, and particle surface properties are most important. Local velocity affects the particle binding through two competing mechanisms: high fluid velocity brings more

particles into a unit structural cell per unit time; on the other hand high local fluid velocity yields greater lift force that keeps particle away from a solid surface. Our simulation results show that the latter dominates and the deposition rate coefficient decreases with fluid velocity for various particle surface potentials and tissue porosities. The repulsive electrostatic force plays an important role in keeping the particles from binding to the cell surfaces. Proper coating of the particles is an important means to avoid nanoparticle accumulation at the injection site. Larger tissue porosity is associated with larger pore size and larger distance between the cells. The deposition rate coefficient decreases substantially with increase in porosity, especially for lower velocities.

Tissue deformation can significantly affect the transport of nanoparticle during an infusion process. First, the particle distribution is not symmetrically spherical due to the presence of the needle and tissue deformation. In fact, the tissue on the outer surface of the needle recedes under the infusion pressure and forms an annular space. Nanofluid fills the annular space and serves as an extra source for nanoparticles to infiltrate through the tissue. The length of the backflow is dependent on infusion rates, needle sizes, tissue properties [36, 55]. Higher infusion rates yield three consequences: a longer backflow length and spreading of the particles along the needle track, a lower deposition rate coefficient, and larger tissue porosity near the needle tip. All these contribute to reducing particle deposition at the needle tip. As a result, high infusion rates lead to a deeper particle penetration and lower particle concentration at the injection site. The relationship of the particle penetration depth to the infusion rates observed in this study is consistent with previous micro-CT imagining results and measurement of *SAR* in gels and tissues [3, 48, 49].

Needle size is another important parameter in intratumoral infusion. Given the infusion rate, it is the needle size that defines the infusion pressure and velocity of the infusate at the needle tip. In fact, large-gauge needles that have a smaller diameter result in a higher infusion pressure at the needle tip. The elevated infusion pressure causes higher velocity and more enlarged pore size near the needle tip, both facilitating particle infiltration into tissue. Also, a smaller needle size can cause a shorter backflow length which is more favorable in confining therapeutic agents inside of a tumor. It should be noted that the reduced needle size only affects an area in the close vicinity of the needle tip and the elevated infusion pressure may cause tumor breakage.

The response of tissue to infusion pressure is largely dependent on the tissue elastic properties such as Young's modulus. Stiffer tissue does not allow substantial swelling of the pore. Thereby, more nanoparticles are intercepted by the cellular structure near the needle tip. Tissue elastic properties should be considered when selecting infusion parameters. Increasing the injection amount can enhance the nanoparticle concentration in the tumor. However, most nanoparticles will be confined in the tumor if the leakage due to backflow can be minimized.

Since nanoparticle transport in biological tissue is such a complex issue, a number of simplifications were made when developing this multiscale model. One major assumption is that the hindrance of extracellular matrix to particle transport is neglected when predicting the deposition rate coefficient. Consequently, the prediction made by this model may overestimate the particle penetration depth. On the other hand, the effect of available binding sites on the cell surfaces is not considered in the model although it

might limit the rate of particle binding to the cell surface [37]. Neglecting the availability of the binding sites may cause overestimation of the particle deposition on the cell surface. In addition, the physicochemical theory underlying the calculation of particle interaction with the cell surface insofar shares the general properties of all colloidal particles. However, the interaction of particles with the living cells is of course more complex than that of non-living, inert, smooth, and spherical bodies. Besides, the complex cellular structure renders the flow path tortuous and the random packing of the cells causes some volume fraction inaccessible to nanoparticles. It should also be noted that in the currently model, dilute nanofluid is employed and particle agglomeration is not considered. It is unclear to what extent the particle-particle interactions affect the particle transport, especially when highly concentrated nanofluids are employed. These limitations should be addressed in the future through united experimental and theoretical study.

The poroelastic model developed in this study is limited to spherical tumor, homogenous media and isotropic deformation. However, nanofluid transport in tumor and the ultimate nanofluid distribution are dependent on the heterogeneous and anisotropic tissue properties, irregular tumor shape, and cracks and necrotic tissues which are common features in large tumors. Also, elevated infusion pressures may break tumors and cause the formation of cracks during infusion. These mechanisms should be included in the model in future studies.

Despite the assumptions used in this study, the simulation predicts the penetration depth at the same order of magnitude as those obtained through micro-CT imaging [3] and indicated by *SAR* measurements [48, 49], suggesting that the modeling framework presented in this study captures the main features of the complex process of nanoparticle transport in tissues. A quantitative relationship among fluid flow, tissue deformation, nanoparticle deposition, and nanoparticle transport is established and the effects of major infusion parameters on nanoparticle distribution are characterized.

7. CONCLUSION

In nanoparticle hyperthermia, controlling the nanoparticle distribution delivered in tumors is vital for achieving an optimum distribution of temperature elevations that enables a maximum damage of the tumor cells while minimizing the heating in the surrounding healthy tissues. A multi-scale model was developed in this study to investigate the spatial concentration distribution of nanoparticles in tissues after intratumoral infusion. Simulations were performed to quantify the effects tumor deformation and particle binding to the cellular structure on the behavior of particle transport. The results show that the rate of particle binding to the cell surface can be reduced by increasing the interstitial fluid velocity, tissue porosity, and surface charge of the particles. Tissue deformation induced by the infusion pressure causes backflow and change in tissue porosity near the needle tip, which substantially affects the distribution and penetration depth of the nanoparticles. Higher infusion rates, larger needle sizes and lower values of Young's modulus yield longer backflow length. On the other hand, high infusion rates, small needle sizes, and low values of Young's modulus reduce

nanoparticle deposition near the injection site. The nanoparticle concentration in tumor can be increased if more nanofluid is infused.

The current study will continue by progressively including further considerations such as heterogeneous porous structure, presence and formation of cracks in tumor, and correction factors for the deposition rate coefficient to address the limitations of the current model. We anticipate that continuous improvement in the model will advance design of treatment protocols for large-sized, irregular-shaped tumors using nanoparticle hyperthermia.

ACKNOWLEDGEMENT

NOMENCLATURE

A potential
b radius of the fluid shell shown in Fig. 1
F shape factor in Eq. (8)
C molar concentration of the particles in the fluid
a_c cell diameter
d_p particle diameter
e dilatation
D diffusion coefficient
E Young's modulus
$\mathbf{F}$ forces acting on the particle
G Lamé constants
h distance between the particle centre and the wall
I electron charge
K permeability of the tissue
k_f deposition rate coefficient
k_B Boltzmann's constant
m mass
M material constant in Eq. (6)
p_f fluid pressure
$\mathbf{r}$ displacement of particle
S volumetric concentration of the nanoparticles bounded to the solid structure
T absolute temperature
t time
$\mathbf{u}$ displacement vector of solid structure
$\mathbf{v}$ interstitial fluid velocity vector
x, y particle position

Greek Symbols

γ	thickness of the fluid layer
ε	porosity
ε_0	vacuum permittivity/initial porosity
ε_r	relative dielectric constant of the water
ξ	uniformly distributed random number
η_s	collector efficiency
θ	valence of the electrolyte
κ	Debye-Hückel parameter
λ	Lamé constant
μ	viscosity of the fluid
ρ	density
τ	tortuosity
υ	Poisson ratio

REFERENCE

1. P. Adomeit and U. Renz, Correlation for the particle deposition rate accounting for lift forces and hydrodynamic mobility reduction, *Can J Chem Eng*, vol. 78, pp. 32–39, 2000.
2. E. Allard, C. Passirani, and J.P. Benoit, Convection-enhanced delivery of nanocarriers for the treatment of brain tumors, *Biomaterials*, vol. 30 (12), pp. 2302-2318, 2009.
3. A. Attaluri, R. Ma, Y. Qiu, W. Li, and L. Zhu, Nanoparticle distribution and temperature elevations in prostatic tumors in Mice during magnetic nanoparticle hyperthermia, submitted to Int J Hyperth, 2011
4. PJ. Basser, Interstitial pressure, volume, and flow during infusion into brain tissue, *Microvascular Research*, vol.(44), pp143-165, 1992.
5. RJ. Bernardi, AR. Lowery, PA. Thompson, SM., Blaney, and JL. West, Immunonanoshells for targeted photothermal ablation in medulloblastoma and glioma: an in vitro evaluation using human cell lines, *J. Neurooncol.,* vol. 86, pp.165-172, 2008.
6. RH. Bobo, D.W. Laske, A. Akbasak, P.F. Morrison, R.L. Dedrick, and E.H. Oldfield, Convection-enhanced delivery of macromolecules in the brain, *Proc Natl Acad Sci USA*, vol. 91(6), pp. 2076–2080, 1994.
7. XM. Chen and M. Sarntinoranont, Biphasic finite element model of solute transport for direct infusion into nervous tissue, *Annuals of Biomedical Engineering*, vol. 35(12), pp. 2145-2158, 2007.
8. ZJ. Chen, W.C. Broaddus, R.R. Viswanathan, R. Raghavan, and G.T. Gillies, Intraparenchymal drug delivery via positive-pressure infusion: experimental and modeling studies of poroelasticity in brain phantom gels, *IEEE Transactions on Biomedical Engineering,* vol. 49(2), 2002.
9. APC. Choi and YP Zheng, Estimation of Young's modulus and poisson's ratio of soft tissue from indentation using two different-sized indentors: Finite element analysis of the finite deformation effect, Med. & Bio. Eng. & Comp., vol. 43, pp. 258-264, 2005.

10. RG. Cox and SK. Hsu, The lateral migration of solid particles in a laminar flow near a plane, *Int J Multiph Flow*, vol. 3(3), pp. 201–222, 1977.

11. LE. Dillehay, Decreasing resistance during fast infusion of a subcutaneous tumor, *Anticancer Res*, vol. 17(1A), pp. 461–466, 1997.

12. IH. El-Sayed, X. Huang, and MA. El-Sayed, Selective laser photo-thermal therapy of epithelial carcinoma using anti- EGFR antibody conjugated gold nanoparticles, *Cancer Letter*, vol. 239, pp. 129-135, 2006.

13. RK. Gilchrist, R. Medal, WD. Shorey, RC. Hanselman, JC. Parrott, and CB. Taylor, Selective inductive heating of lymph nodes, *Ann Surg.*, vol. 146(4), pp. 596–606, 1957.

14. TT. Goodman, J. Chen, K. Matveev, and SH. Pun, Spatio-temporal modeling of nanoparticle delivery to multicellular tumor spheroids, *Biotechnol Bioeng,* vol. 101(2), pp. 388–399, 2008.

15. WY. Gu, H. Hao, CY. Huang, and HS. Cheung, New insight into deformation-dependent hydraulic permeability of gels and cartilage, and dynamic behavior of agarose gels in confined compression, *J. Biomech.*, vol. 36(4), pp. 593-598, 2003.

16. J. Happel, Viscous flow in multiparticle systems: slow motion of fluids relative to beds of spherical particles, *AIChE J*, vol. 4, pp. 197–201, 1958.

17. I. Hilger, R. Hergt, and WA. Kaiser, Towards breast cancer treatment by magnetic heating, *J Magn Magn Mater,* vol. 293(1), pp. 314–319, 2005.

18. I. Hilger, W. Andra, R. Hergt, R. Hiergeist, H. Schubert, and WA. Kaiser, Electromagnetic heating of breast tumors in interventional radiology: in vitro and in vivo studies in human cadavers and mice, *Radiology*, vol. 218(2), pp. 570–575, 2001.

19. MH. Holmes and V.C. Mow, The nonlinear characteristics of soft gels and hydrated connective tissues in ultrafiltration, *Journal of Biomechanics*, vol. 23(11), pp. 1145-1156, 1990.

20. JN. Israelachvili, Intermolecular and surface forces, Academic Press, London, 1991.

21. O. Ivanchenko, N. Sindhwani, and A. Linninger, Experimental Techniques for Studying Poroelasticity in Brain Phantom Gels Under High Flow Microinfusion, *J of Biomechanical Engineering-Transactions of the ASME*, vol. 132 (5), 2010.

22. RK. Jain, Delivery of molecular and cellular medicine to solid tumors, *Adv Drug Deliv Rev*, vol. 26(2–3), pp. 71–90, 1997.

23. A. Jordan, R. Scholz, K. Maier-Hauff, FKH. van Landeghem, N, Waldoefner, U. Teichgraeber, J. Pinkernelle, H. Bruhn, F. Neumann, B. Thiesen, A. von Deimling, and R. Felix, The effect of thermotherapy using magnetic nanoparticles on rat malignant glioma, *J Neuro-Oncol*, vol. 78(1), pp. 7–14, 2006.

24. R. Johnson, The handbook of fluid dynamics, *CRC Press, Boca Raton,* pp. 18-29–18-32, 1998.

25. A-RA. Khaled and K. Vafai, The role of porous media in modeling flow and heat transfer in biological tissues, *Int J Heat Mass Transf*, vol. 46(26), pp. 4989–5003, 2003.

26. B. Khlebtsov, V. Zharov, A. Melnikov, V. Tuchin , and N. Khlebtsov , Optical amplification of photothermal therapy with gold nanoparticles and nanoclusters, *Nanotechnology*, vol. 17 (20), pp. 5167-5179, 2006.

27. PE. Kloeden and E. Platen, Numerical solution of stochastic differential equations, *Springer, Berlin*, pp. 110–154, 1992.

28. WM. Lai and VC. Mow, Drug-induced compression of articular cartilage during a permeation experiment, *Biorheology*, vol. 17, pp. 111-123, 1980.
29. FJ. Lazaro, AR. Abadia, MS. Romero, L. Gutierrez, J. Lazaro, and MP. Morales, Magnetic characterisation of rat muscle tissues after subcutaneous iron dextran injection, *Biochim Biophys Acta Mol Basis Dis,* vol. 1740(3), pp. 434–445, 2005.
30. R. Maniero and P. Canu, A model of fine particles deposition on smooth surfaces: I—theoretical basis and model development, *Chem Eng Sci*, vol. 61(23), pp. 7626–7635, 2006.
31. JP. Matas, JF. Morris, and E. Guazzelli, Lateral forces on a sphere, *Oil Gas Sci Technol – Rev Inst Fr Pet,* vol. 59(1), pp. 59–70, 2004.
32. H. Matsuki, T. Yanada, T. Sato, K. Murakami, and S. Minakawa, Temperature-sensitive amorphous magnetic flakes for intratissue hyperthermia, *Mater Sci Eng*, vol. A181(182), pp. 1366–1368, 1994.
33. S. McGuire and F. Yuan, Quantitative analysis of intratumoral infusion of color molecules, *Am J Physiol Heart Circ Physiol,* vol. 281(2), pp. H715–H721, 2001.
34. S. McGuire, D. Zaharoff and F. Yuan, Nonlinear dependence of hydraulic conductivity on tissue deformation during intratumoral infusion, *Annals of Biomedical Engineering,* vol. 34(7), pp. 1173-1181, 2006.
35. P. Moroz, SK. Jones, and BN. Gray, Magnetically mediated hyperthermia: current status and future directions, *Int J Hyperth*, vol. 18(4), pp. 267–284, 2002.
36. PF. Morrison, MY. Chen, RS. Chadwick, RR. Lonser, and EH. Oldfield, Focal delivery during direct infusion to brain: role of flow rate, catheter diameter, and tissue mechanics, *American J of Physiology-regulatory integrative and Comparative Physiology*, vol. 277(4), pp. R1218-R1229, 1999.
37. KB. Neeves, AJ. Sawyer, CP. Foley, WM. Saltzman, and WL. Olbricht, Dilation and degradation of the brain extracellular matrix enhances penetration of infused polymer nanoparticles, *Brain Research*, vol. 1180, pp. 121-132, 2007.
38. KE. Nelson and TR. Ginn, Colloid filtration theory and the Happel sphere-in-cell model revisited with direct numerical simulation of colloids, *Langmuir*, vol. 21(6), pp. 2173–2184, 2005.
39. PA. Netti, LT. Baxter, and Y. Boucher, Macro-and microscopic fluid transport in living tissues: application to solid tumors, *Bioengineering, Food and Natural Products*, vol. 43(3), pp. 818-834, 1997.
40. CR. O'Melia and W. Stumn, Theory of water filtration, *J. Am. Water Works Assoc.* vol. 59, pp. 1393-1412, 1967.
41. DP. O'Neal, LR. Hirsch, NJ. Halas, JD. Payne, and JL. West, Photo-thermal tumor ablation in mice using near infrared-absorbing nanoparticles, *Cancer Letters*, vol. 209, pp. 171-176, 2004.
42. R. Raghavan, S. Mikaelian, M. Brady, and ZJ. Chen, Fluid infusions from catheters into elastic tissue: I. Azimuthally symmetric backflow in homogeneous media, *Phys. Med. Biol.* , vol. 55, pp. 281-304, 2010.
43. R. Rajagopalan, and C. Tien, Trajectory analysis of deep-bed filtration with sphere-in-cell porous media model, *AIChE J*, vol. 22(3), pp. 523–533, 1976.
44. S, Ramanujan, A. Pluen, TD. McKee, EB. Brown, Y. Boucher, and RK. Jain, Diffusion and convection in collagen gels: implications for transport in the tumor interstitium, *Biophys J.*, vol. 83(3), pp. 1650–1660, 2002.

45. BV. Ramarao, C. Tien, and S. Mohan, Calculations of single fiber efficiencies for interception and impaction with superposed Brownian motion, *J Aerosol Sci,* vol. 25(2), pp. 295–313, 1994.
46. W. Russel, AD. Saville, and W. Schowalter, Colloidal dispersions, Cambridge University Press, UK, 1989.
47. PG. Saffman, The lift on a small sphere in a slow shear flow, *J Fluid Mech Digit Arch*, vol. 22, pp. 385–400, 1965.
48. M. Salloum, RH. Ma, D. Weeks, and L. Zhu, Controlling nanoparticle delivery in magnetic nanoparticle hyperthermia for cancer treatment: experimental study in agarose gel, *Int J Hyperth*, vol. 24(4), pp. 337–345, 2008a.
49. M. Salloum, RH. Ma, and L. Zhu, An in-vivo experimental study of temperature elevations in animal tissue during magnetic nanoparticles hyperthermia, *Int J Hyperth*, vol. 24(7), pp. 589-601, 2008b.
50. M. Salloum, RH. Ma, and L. Zhu, Enhancement in treatment planning for magnetic nanoparticle hyperthermia: Optimization of the heat absorption pattern, *Int J Hyperth*, vol. 25(4), pp. 309-321, 2009.
51. CN. Satterfield, Mass transport in heterogeneous catalysis, MIT Press, Cambridge, 1970.
52. S.E. Skrabalak, J. Chen, L. Au and X. Lu, Gold nanocages for biomedical applications, *Adv. Mater. Deerfield* , vol. 19, pp. 3177–3184. 2007.
53. I. Sobey and B. Wirth, Effect of non-linear permeability in a spherically symmetric model of hydrocephalus, *Mathematical medicine and biology*, vol. 23(4), pp. 339-361, 2006.
54. D. Su, RH. Ma, M. Salloum, and L. Zhu, Multi-scale study of nanoparticle transport and deposition in tissues during an injection process, *Med Biol Eng Comput,* vol. 48, pp. 853–863, 2010.
55. D. Su, RH. Ma, and L. Zhu, Numerical study of nanofluid infusion in deformable tissue during hyperthermia treatment of cancers, *Med Biol Eng Comput,* submitted, 2011.
56. K. Subramani, H. Hosseinkhani, A. Khraisat, M. Hosseinkhani, and Y. Pathak, Targeting Nanoparticles as Drug Delivery Systems for Cancer Treatment, Current nanoscience, vol. 5 (2), pp. 135-140, 2009.
57. MA. Swartz and ME Fleury, Interstitial flow and its effects in soft tissues, *Annu. Rev. Biomed. Eng.*, vol. (9), pp.229-256, 2007.
58. C. Tien and BV. Ramarao, Granular filtration of aerosols and hydrosols, 2nd edn. Elsevier, Oxford, 2007.
59. N. Tufenkji and M. Elimelech, Correlation equation for predicting single-collector efficiency in physicochemical filtration in saturated porous media, *Env Sci Technol,* vol. 38(2), pp. 529–536, 2004.
60. M. Wang and M. Thanou, Targeting nanoparticles to cancer, *Pharmacological Research*, vol. 62, pp. 90–99, 2010.
61. Y. Wang, H. Wang, CY. Li, F. Yuan, Effects of rate, volume, and dose of intratumoral infusion on virus dissemination in local gene delivery, *Mol Cancer Ther*, vol. 5(2), pp. 362–366, 2006.
62. P. Warszynski, Coupling of hydrodynamic and electric interactions in adsorption of colloidal particles, *Adv Colloid Interface Sci,* vol. 84(1–3), pp. 47–142, 2000.